ACS APPLIED ENERGY MATERIALS

www.acsaem.org Article

Tunable Pyridyl-Based Conjugated Microporous Polymers for Visible Light-Driven Hydrogen Evolution

Mohammed G. Kotp,[▽] Ahmed M. Elewa,[▽] Ahmed F. M. EL-Mahdy,* Ho-Hsiu Chou,* and Shiao-Wei Kuo*

Cite This: *ACS Appl. Energy Mater.* 2021, 4, 13140−13151 Read Online

ACCESS | Metrics & More | Article Recommendations | Supporting Information

ABSTRACT: Conjugated microporous polymers (CMPs) are promising light harvesters for photocatalytic H_2 evolution because they are simple to prepare with various band gaps. To achieve CMPs displaying high photocatalytic performance, appropriate building blocks must be chosen. We prepared four kinds of triphenylpyridine-based CMPs (TPP-CMPs) through reactions with multibrominated monomers having different geometries [1,3,6,8-tetrabromopyrene (pyrene-4Br), tris(4-bromophenyl)amine (TPA-3Br), 2,4,6-tris(4-bromrophenyl)-pyridine (TPP-3Br), and 1,2,4,5-tetrabromobenzene (BZ-4Br), forming the TPP-pyrene (Py), TPP-triphenylamine (TPA), TPP-TPP, and TPP-benzene (BZ) CMPs, respectively]. This strategy allowed effective synthetic regulation of electron enrichment, porosities, and optoelectronic properties of the TPP-CMPs. The surface areas of the TPP-CMPs were high, up to 1370 $m^2\ g^{-1}$, and had a high thermal stability. TPP-Py CMP displayed the highest photocatalytic performance with a H_2 production rate of 18 100 μmol $g^{-1}\ h^{-1}$ under irradiation with visible light. Moreover, we achieved apparent quantum yields as high as 22.97% at 420 nm, comparable with those of most other CMPs reported previously.

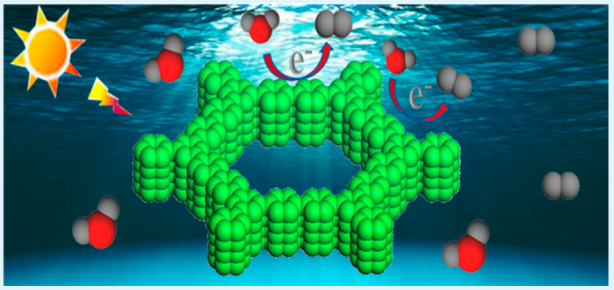

KEYWORDS: *conjugated microporous polymer, H_2 evolution, photocatalytic, triphenylpyridine, triphenylamine*

INTRODUCTION

Photocatalysis has attracted attention recently for its great potential to solve environmental problems by using clean and abundant solar energy.[1,2] Over the past decade, the development of efficient photocatalytic systems capable of converting solar energy into chemical fuels has attracted significant interest. Since Fujishima and Honda reported a TiO_2 photocatalyst for photocatalytic H_2 evolution,[3] great efforts have been made to search for ideal photocatalysts for H_2 evolution. Although most of these photocatalysts have been inorganic materials,[4−6] organic polymers have received increasing interest after graphitic carbon nitride (g-C_3N_4) was reported to be photocatalytically active for water splitting.[7] Organic polymer-based semiconductors are interesting photocatalysts because their optical and electronic properties can be adjusted readily by changing their basic building blocks.[8−10] Accordingly, several conjugated organic photocatalysts that mediate photocatalytic H_2 production from water under visible light have been reported, including linear polymers,[9−12] polymer dots,[13−16] hydrophilic polymers,[17−19] covalent triazine frameworks,[20,21] and covalent organic frameworks (COFs).[22−26] Recently, conjugated microporous polymers (CMPs) have become promising materials for effective photocatalysts of H_2 evolution because of their high surface areas, diverse compositional strategies, high charge mobilities, and controllable band gaps with their chemical structures and electronic properties amenable to precise customization.[27−35]

CMPs were first prepared by the Cooper group[42,43] and have since undergone great development.[36] These porous polymeric materials have attracted great attention as alternatives to covalent COFs and metal−organic frameworks for gas sensing, gas storage, and catalysis and for their use in supercapacitors and rechargeable batteries.[37−41] CMPs have displayed high tolerance and robustness toward various chemical and thermal environments. Recently, the Cooper group reported a series of CMPs based on pyrene building blocks for effective H_2 evolution under visible light; the optical band gap could be finely tuned over the range from 1.94 to 2.95 eV by changing the monomer composition of these CMPs.[42] The same group also compared a range of porous network polymers and nonporous linear polymers, on the basis of either fluorene or dibenzo[*b*,*d*]thiophene units, as photocatalysts for H_2 production from water in the presence of a sacrificial hole scavenger.[43] The H_2 evolution rates of the

Received: September 7, 2021
Accepted: October 12, 2021
Published: October 29, 2021

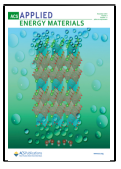

https://doi.org/10.1021/acsaem.1c02772
ACS Appl. Energy Mater. 2021, 4, 13140−13151

porous network polymers outperformed those of their linear structural analogues. Furthermore, CMP frameworks derived from pyridine derivatives have displayed excellent electron affinities and electron transfer properties due to their aromatic heterocyclic units being electron deficient[44−46] with the nitrogen atom of the pyridine ring playing an important role because its lone pair of electrons is localized in an sp^2-hybridized orbital, contributing to active reaction sites.[46−48] Therefore, we became interested in the incorporation of triarylpyridine units in polymeric frameworks. To the best of our knowledge, the fabrication of CMPs based on triphenylpyridine (TPP) is rare for photocatalytic hydrogen evolution from water. Zhu and co-workers synthesized pyridyl-functional conjugated polymers via a rapid, metal-free synthetic approach to visible light water splitting,[49] but we are unaware of any previous studies of pyridine-based CMPs for photocatalytic H_2 evolution prepared from comonomer building blocks having a variety of electron richness, planarities, and electronic structures. Whereas pyrene (Py) and triphenylamine (TPA) have higher electron enrichment than TPP or benzene (BZ),[50−52] on close a scale, Py has higher planarity than TPA, and TPP has higher planarity than BZ. Because photoluminescent materials are welcomed in photochromic devices, Py and TPA moieties are particularly interesting for use in, for example, solar cells[53] and photosensors[54] due to their ability to release cationic radicals upon oxidation with subsequent color variation.[55]

In this study, we prepared pyridyl-based boronic ester, 2,4,6-tris(4-(4,4,5,5-tetramethyl-1,3,2-dioxaborolan-2-yl)phenyl) pyridine (TPP-3BO), and used it as a building block for tuning and construction four novel CMPs of various planarities and electron enrichments (TPP-Py, TPP-TPA, TPP-TPP, TPP-BZ CMPs) for the photocatalytic H_2 evolution from water. We examined the structure−function relationships of these pyridine-based CMPs by varying their linkers and analyzing the effects of the electronic structures and geometries of the monomers, showing that the emission spectra, and hence the optical gap, can be tuned over a wide range. Interestingly, these four CMPs displayed high luminescence stabilities, high Brunauer−Emmett−Teller (BET) surface areas, and high thermal stabilities and photocatalytic hydrogen evolution from water in the presence of a sacrificial electron donor.

EXPERIMENTAL SECTION

Materials. The practical section for this research employed a variety of chemicals from an analytical class as well as introduced experiments without supplementary purification. Palladium-tetrakis-(triphenylphosphine) ($pd(pph_3)_4$), potassium acetate, and potassium carbonate (K_2CO_3) were delivered from Combi-Blocks (San Diego, USA). Tetrakis(triphenylphosphine)palladium was purchased from Acros. [1,1′-Bis(diphenylphosphino)ferrocene]dichloropalladium(II), dioxane, tetrahydrofuran (THF), dimethylactaamide (DMAC), dimethylformamide, and hexane were obtained from Sigma Aldrich. DI water was used for all experiments.

Synthesis of 1,3,6,8-Tetrabromopyrene (Py-4Br). 1,3,6,8-Tetrabromopyrene (pyrene-4Br) was synthesized as described in a previous report.[25] As exhibited in Scheme S1, pyrene (5.0 g, 24 mmol) was added to nitrobenzene (200 mL), followed by dropwise addition of bromine (5.6 mL, 109 mmol). The previously prepared flask was refluxed under 120 °C for 15 h. Pale yellow crystallites of 1,3,6,8-tetrabromopyrene were formed after the consumption of bromine, and then, they were filtered. The precipitate was exposed to washing processes via ethanol and then dried for 12 h under pressure. FTIR: 3078, 1587, 1450, 1228, 1052, 988, 862, 812 cm^{-1} (Figure S1b).

Synthesis of Tris(4-bromophneyl)amine (TPA-3Br). Tris(4-bromophenyl)amine was formed according to the previously reported work.[26] As exhibited in Scheme S2, in a beaker, *N*-bromosuccinimide (NBS; 12 g, 12.32 mmol) was dissolved in DMF (60 mL). Another solution of trimethylamine (5 g, 4.080 mmol) was mixed with DMF (120 mL) at 0 °C. The first solution (NBS) was dropwise added onto the second; then, the mixture was left under stirring at room temperature overnight. The mixture was sedimented via pouring onto cold water and then extracted by DCM, followed by washing several cycles with methanol; white precipitate was formed. FTIR: 3064, 1570, 1266, 1081, 995, and 816 cm^{-1} (Figure S2b). ^1H NMR (400 MHz, 25 °C, CD_3Cl): δ 7.35 (d, J = 8.8, 6H), 6.921 ppm (d, J = 8.8, 6H) (Figure S5). ^{13}C NMR ($CDCl_3$, 25 °C, 500 MHz): 146.7, 132.8, 126.01, and 116.38 ppm (Figure S6).

Synthesis of 2,4,6-Tris(4-bromrophenyl)pyridine (TPP-3Br). 4-Bromoacetophenone was prepared according to a previously published report.[26] As exhibited in Scheme S3, 4-bromoacetophenone (4.14 g, 20.8 mmol), 4-bromobenzaldehyde (1.94 g, 10.4 mmol), ammonium acetate (28.0 g, 363 mmol), and acetic acid (14.6 mL, 0.260 mmol) were added to a 20 mL microwave flask under stirring. The temperature of the previous mixtures was raised to 220 °C for 45 min under self-generated pressure of 500 W. The flask was cooled to room temperature followed by the addition of water. $NaHCO_3$ solution was added in order to neutralize the suspension. DCM was employed for the extraction of the aqueous phase. Finally, under reduced pressure, the solvent was evaporated and then recrystallized and dried under vacuum. FT-IR (powder): 3064, 1596, 1544, 1538, 1500, 1420, 1376, 1177, 1067, 1007, 813, 489 cm^{-1} (Figure S3b). ^1H NMR ($CDCl_3$, 25 °C, 600 MHz): δ 8.037 (d, 4H), 7.8 (s, 2H), 7.647 (d, 2H), 7.65 (d, 4H), 7.58 ppm (d, 2H) (Figure S7). ^{13}C NMR ($CDCl_3$, 25 °C, 500 MHz): δ 156.5, 149.5, 137.84, 137.28, 132.28, 131.82, 128.5, 123.9, 123.5, and 116.73 ppm (Figure S8).

Synthesis of 2,4,6-Tris(4-(4,4,5,5-tetramethyl-1,3,2-dioxaborolan-2-yl)phenyl)pyridine (TPP-3BO). TPP-3BO is synthesized through boronation of TPP-3Br (Scheme S4). In a two-neck flask, 2,4,6-tris(4-bromophenyl)pyridine (2.20 mmol, 1.2 g) was added to bis(pinacolato)diboron (10.12 mol, 2.57 g), [1,1′-bis(diphenylphosphino)ferrocene]dichloropalladium(II) ($Pd(dppf)_2Cl_2$) (0.193 mmol, 0.142 g), and potassium acetate (9.15 mmol, 0.9 g). The mixture was degassed before solvent addition for 15 min. 50 mL of dioxane was injected into the flask, and the flask was left under magnetic stirring and a nitrogen atmosphere for another 2 days under 110 °C in a silicone oil bath. The black solution was collected onto ice water and then filtered and washed well. Column chromatography with an eluent of THF/hexane (1:3) was used to obtain the white substrate after rotary evaporation of the effluent. Afterward, the crude was soaked in methanol for one night for complete purification, and then, it was dried at 50 °C for 10 h. It is worth noting that boron matrixes were kept in the fridge for further use. FTIR (powder): 2980, 1613, 1534, 1399, 1355, 1212, and 1141 cm^{-1} (Figure S1a). ^1H NMR (400 MHz, 25 °C, CD_3Cl): δ 8.2 (d, J = 8.8, 4H), 7.9 (d, J = 8.8, 2H), 7.93 (s, 2H), 7.75 (d, 4H), 1.37 ppm (s, 12H) (Figure S9). ^{13}C NMR ($CDCl_3$, 25 °C, 500 MHz): δ 158.4, 150.6, 142.2, 136.1, 127.7, 118.4, 84.79, and 24.69 ppm (Figure S10). HRMS (ESI): m/z calculated for $C_{41}H_{50}B_3NO_6$: 686.4; found: 686.4 (as clarified in Figure S11).

Synthesis of TPP-Pyrene Conjugated Microporous Polymer (TPP-PY CMP). In a specially designed tube (that is able to withstand the high evacuation force), TPP-3BO (0.38 mmol, 264.6 mg) and 4-bromopyrene (0.29 mmol, 150 mg) were mixed together. $Pd(pph_3)_4$ (0.03 mmol, 35 mg) in addition to potassium carbonate (2.9 mmol, 400 mg) was supplemented in the tube. The above-mentioned solid materials were degassed for 15 min to complete the removal of any dissolved solvents. After that, DMF (10 mL) and water (1.25 mL) were injected into the tube. Through liquid nitrogen, the tube contents were frozen; then, a degasification process for its contents was done again (freeze−pump−thaw). This freeze−pump−thaw was applied for three cycles (15 min per each cycle). The tube was heated in a silicone oil bath for 3 days at 150 °C under magnetic stirring. After 3 days, the contents of the tube were poured onto ice and water

https://doi.org/10.1021/acsaem.1c02772
ACS Appl. Energy Mater. 2021, 4, 13140−13151

Scheme 1. Synthesis and Structures of the Four New CMPs Solvated in DMF at 140 °C and a Nitrogen Atmosphere

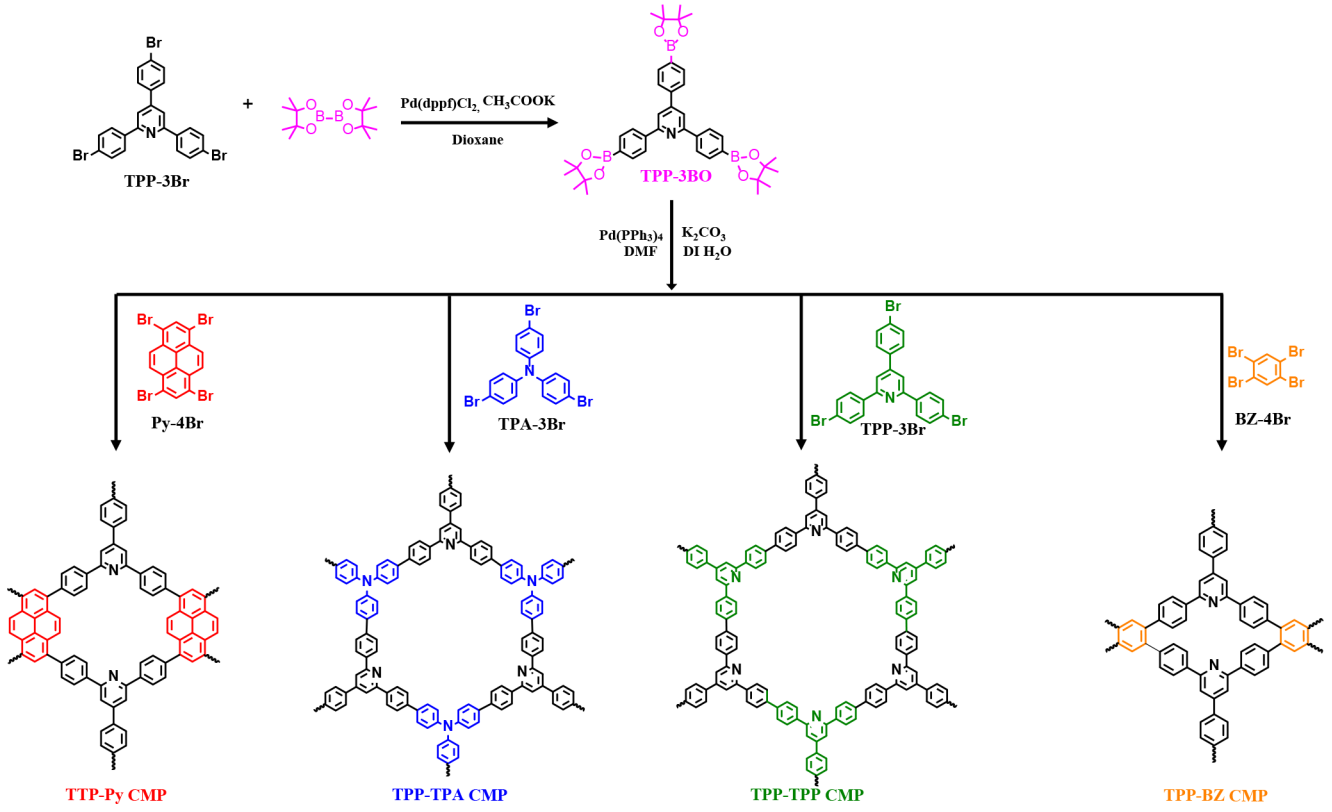

to form the precipitate. A centrifuge machine was utilized for precipitate separation. Water, acetone, and methanol were employed to purify the precipitate with 3 washing steps. Then, the moiety was dried at 100 °C for a day (Scheme S5).

Synthesis of TPP-Triphenylamine Conjugated Microporous Polymer (TPP-TPA CMP). In a specially designed tube (that is able to withstand the high evacuation force), TPP-3BO (0.31 mmol, 214 mg) and TPA-3Br (0.31 mmol, 150 mg) were mixed together. $Pd(pph_3)_4$ (0.03 mmol, 35 mg) in addition to potassium carbonate (3.1 mmol, 430 mg) were supplemented in the tube. The above-mentioned solid materials were degassed for 15 min to complete the removal of any dissolved solvents. After that, DMF (10 mL) and water (1.25 mL) were injected into the tube. Through liquid nitrogen, the tube contents were frozen; then, a degasification process for its contents was done again (freeze−pump−thaw). This freeze−pump−thaw was applied for three cycles (15 min per each cycle). The tube was heated in a silicone oil bath for 3 days at 150 °C under magnetic stirring. After 3 days, the contents of the tube were poured onto ice and water to form the precipitate. A centrifuge machine was applied for precipitate separation. Water, acetone, and methanol were employed to purify the precipitate with 3 washing steps. Then, the moiety was dried at 100 °C for a day (Scheme S6).

Synthesis of TPP-TPP Conjugated Microporous Polymer (TPP-TPP CMP). In a specially designed tube (that is able to withstand the high evacuation force), TPP-3BO (0.27 mmol, 189 mg) and TPP-3Br (0.27 mmol, 150 mg) were mixed together. $Pd(pph_3)_4$ (0.03 mmol, 35 mg) in addition to potassium carbonate (2.75 mmol, 381 mg) were supplemented in the tube. The above-mentioned solid materials were degassed for 15 min to complete the removal of any dissolved solvents. After that, DMF (10 mL) and water (1.25 mL) were injected into the tube. Through liquid nitrogen, the tube contents were frozen; then, a degasification process for its contents was done again (freeze−pump−thaw). This freeze−pump−thaw was applied for three cycles (15 min per each cycle). The tube was heated in a silicone oil bath for 3 days at 150 °C under magnetic stirring. After 3 days, the contents of the tube were poured onto ice and water to form the precipitate. A centrifuge machine was applied for precipitate separation. Water, acetone, and methanol were employed to purify the precipitate with 3 washing steps. Then, the moiety was dried at 100 °C for a day (Scheme S7).

Synthesis of TPP-BZ Conjugated Microporous Polymer (TPP-BZ CMP). In a specially designed tube (that is able to withstand the high evacuation force), TPP-3BO (0.39 mmol, 232.1 mg) and 1,2,4,5-tetrabromobenzene (0.25 mmol, 100 mg) were mixed together. $Pd(pph_3)_4$ (0.03 mmol, 35 mg) in addition to potassium carbonate (2.54 mmol, 352 mg) were supplemented in the tube. The above-mentioned solid materials were degassed for 15 min to complete the removal of any dissolved solvents. After that, DMF (10 mL) and water (1.25 mL) were injected into the tube. Through liquid nitrogen, the tube contents were frozen; then, a degasification process for its contents was done again (freeze−pump−thaw). This freeze−pump−thaw was applied for three cycles (15 min per each cycle). The tube was heated in a silicone oil bath for 3 days at 150 °C under magnetic stirring. After 3 days, the contents of the tube were poured onto ice and water to form the precipitate. A centrifuge machine was applied for precipitate separation. Water, acetone, and methanol were employed to purify the precipitate with 3 washing steps. Then, the moiety was dried at 100 °C for a day (Scheme S8).

RESULTS AND DISCUSSION

Synthesis and Characterization of CMPs. The porosity, specific surface area, and thermal stability of porous organic polymers can be affected by the flexibility and versatility of their building blocks and linkers. In addition, because the nitrogen atoms of tertiary amino and pyridyl units feature a free electron pair, TPA and TPP units can serve as active redox sites for important photo- and electrochemical reactions. Benzene and pyrene moieties are aromatic systems that generally undergo strong stacking stabilized through $\pi-\pi$ interactions. Therefore, in this study, we investigated the effects of four different monomers displaying different degrees of flexibility and geometric versatility: 1,3,6,8-tetrabromopyr-

https://doi.org/10.1021/acsaem.1c02772
ACS Appl. Energy Mater. 2021, 4, 13140−13151

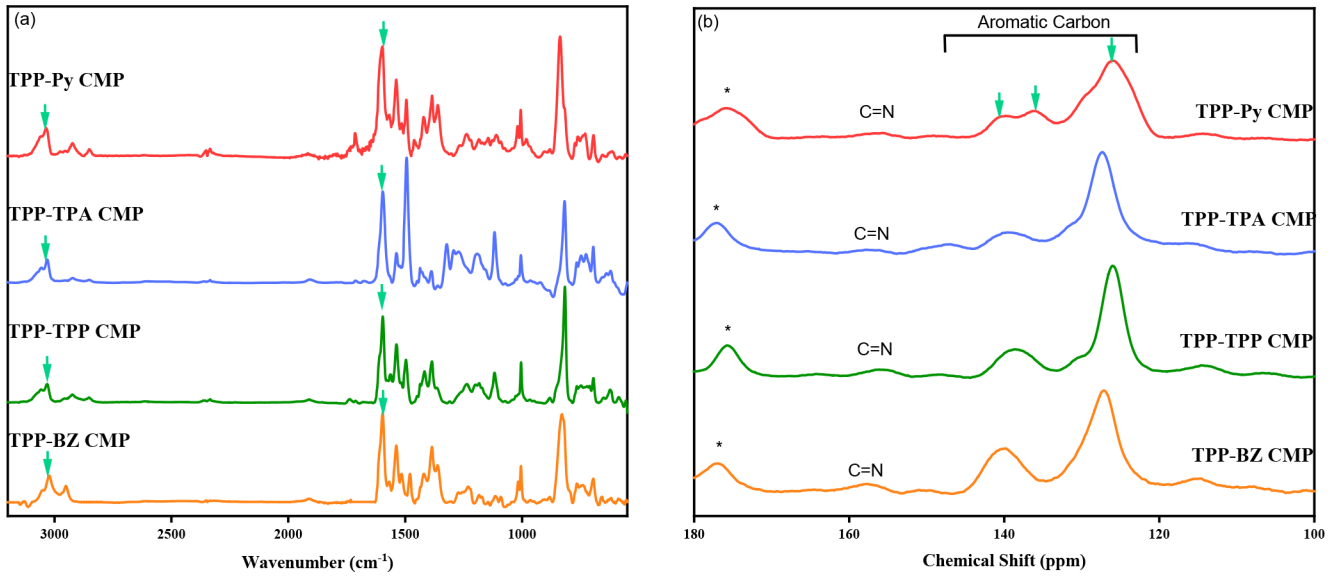

Figure 1. (a) FTIR and (b) solid state ^{13}C NMR spectra of the TPP-Py, TPP-TPA, TPP-TPP, and TPP-BZ CMPs.

ene (Py-4Br), tris(4-bromophenyl)amine (TPA-3Br), 2,4,6-tris(4-bromophenyl)pyridine (TPP-3Br), and 1,2,4,5-tetrabromobenzene (BZ-4Br). We used these compounds to demonstrate the fine-tuning of TPP-Py, TPP-TPA, TPP-TPP, and TPP-BZ CMPs, respectively, and investigated the effects of the nucleophilicity of the nitrogen atoms and the planarity of the building blocks on their porosities, specific surface areas, thermal stabilities, and photophysical properties as well as their ability to mediate photocatalytic H_2 evolution from water.

We synthesized TPP-3BO through the reaction of TPP-3Br with bis(pinacolato)diboron (Scheme S4). Its Fourier transform infrared (FTIR) spectrum (Figure S1a) featured signals for the stretching vibrations of C−H (2980 cm^{-1}), C═N (1613 cm^{-1}), C═C (1534 cm^{-1}), B−O (1399 cm^{-1}), C−B (1212 cm^{-1}), and C−O (1141 cm^{-1}) bonds. The ^{1}H NMR spectrum of TPP-3BO (Figure S9) contained distinct peaks at 1.37 ppm for the methyl protons and 7.96 ppm for the protons located on the pyridyl ring with the remaining signals in the region from 8.2 to 7.75 ppm being those of the protons of the substituted aromatic rings. The signal of the methyl groups of TPP-3BO appeared in the ^{13}C NMR spectrum at 24.76 ppm, along with signals at 84.5 ppm for the central carbon atom between the methyl groups and the boron ring and at 158.4 ppm for the C═N atoms of the pyridine ring; the other peaks at 151, 142.35, 127.08, and 118.23 ppm represented the carbon nuclei of the two aryl rings (Figure S10). Furthermore, the molecular weight was confirmed through mass spectroscopy as clarified in Figure S11.

We employed palladium-catalyzed Suzuki couplings for the synthesis of the TPP-Py, TPP-TPA, TPP-TPP, and TPP-BZ CMPs, as presented in Scheme 1. We performed the reactions in Schlenk tubes while heating over 3 days, providing each of the reaction products in high yield. We characterized the molecular structures of these novel CMPs from FTIR and solid state ^{13}C NMR spectra.

Figure 1a presents the FTIR spectra of the TPP-Py, TPP-TPA, TPP-TPP, and TPP-BZ CMPs, revealing stretching vibrations for the C−H bonds >3000 cm^{-1} and for the C═C bonds near 1609 cm^{-1}. These spectra did not feature any signals for the stretching vibrations of B−O (1400 cm^{-1}), C−B (1200 cm^{-1}), or C−O (1141 cm^{-1}) bonds, confirming the successful synthesis of our CMPs. The solid state ^{13}C NMR spectra of the CMPs (Figure 1b) featured signals in the range of 156.42−157.41 ppm for the pyridyl C═N units in addition to signals for the aromatic carbon nuclei in the ranges of 149.63−113.88, 147.41−114.99, 148.08−113.98, and 150.18−114.77 ppm for the TPP-Py, TPP-TPA, TPP-TPP, and TPP-BZ CMPs, respectively. Thermogravimetric analysis (TGA) under a N_2 atmosphere revealed the high thermal stabilities of our polymers at high temperatures (Figure 2, Table 1).

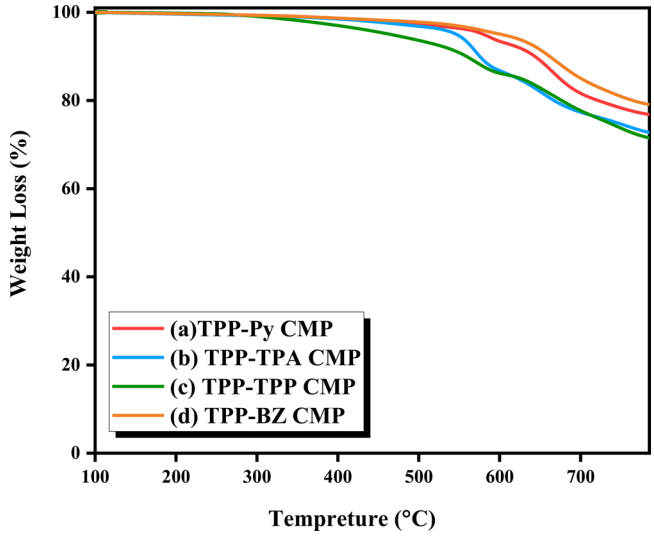

Figure 2. Thermogravimetric analysis trace of (a) TPP-Py, (b) TPP-TPA, (c) TPP-TPP, and (d) TPP-BZ CMPs under a nitrogen atmosphere with a heating rate of 20 °C min^{-1}.

Interestingly, the degree of planarity affected the thermal stabilities. The TPP-Py and TPP-BZ CMPs, formed from most planar linkers (BZ and Py, respectively), had the highest thermal stabilities (characterized by the decomposition temperature T_{d10}) of 654 and 635 °C, respectively, due to the high resulting $\pi-\pi$ stacking; in contrast, the values of T_{d10} of the CMPs based on the less-planar monomers (i.e., the

https://doi.org/10.1021/acsaem.1c02772
ACS Appl. Energy Mater. 2021, 4, 13140−13151

Table 1. Thermal Properties and Porous Properties of These CMPs

CMP	$T_{d10\%}$ (°C)	char yield (%)	S_{BET} (m^2 g^{-1})	pore size (nm)	pore volume (cm^3 g^{-1})
TPP-Py CMP	635	76.7	1160	0.88	0.321
TPP-TPA CMP	570	72.5	540	1.79	0.530
TPP-TPP CMP	548	71.2	640	1.84	0.695
TPP-BZ CMP	654	78.9	1370	1.27	0.411

TPP-TPA and TPP-TPP CMPs) were 570 and 548 °C, respectively. The char yields for the TPP-Py, TPP-TPA, TPP-TPP, and TPP-BZ CMPs after heating to 800 °C were 76.7%, 72.5%, 71.2%, and 78.9%, respectively. Moreover, high thermal stabilities of the four CMPs suggested high degrees of condensation and $\pi-\pi$ stacking.

We performed isothermal N_2 sorption analysis at 77 K to examine the porosity characteristics of our TPP-Py, TPP-TPA, TPP-TPP, and TPP-BZ CMPs. The four CMPs possessed microporous structures, as confirmed by each revealing a sharp N_2 uptake at lower pressure ($P/P_0 < 0.05$) in a type I isotherm (Figure 3a–d). We used the BET method to evaluate the surface areas and pore volumes of the CMPs. The TPP-Py and TPP-BZ CMPs had the highest specific surface areas of 1160 and 1370 m^2 g^{-1}, respectively, but relatively low pore volumes of 0.321 and 0.411 cm^3 g^{-1}, respectively; the TPP-TPA CMP had a surface area of 570 m^2 g^{-1} and a pore volume of 0.53 cm^3 g^{-1}. For the TPP-TPP CMP, these values were 548 m^2 g^{-1} and 0.695 cm^3 g^{-1}, respectively (Table 1). Using nonlocal density functional theory (NLDFT), we calculated the pore size distributions of the TPP-Py, TPP-TPA, TPP-TPP, and TPP-BZ CMPs to be 0.88, 1.79, 1.84, and 1.27 nm as shown in Figure 3e–h, respectively, confirming the microporosity of each CMP (Table 1). Clearly, these CMPs have a high surface area, which leads to a more active site where higher BET surface areas are beneficial to enhance the dispersion of the catalyst and interaction with the reactants, and thus more efficient hydrogen production.

We employed field-emission scanning electron microscopy (FE-SEM; Figure 4a–d) and transmission electron microscopy (TEM; Figure 4e–h) to visualize the morphologies of the TPP-Py, TPP-TPA, TPP-TPP, and TPP-BZ CMPs. These synthesized CMPs possessed spherical microstructures. The TEM images in Figure 4e–h revealed smooth surfaces for the TPP-Py, TPP-TPA, TPP-TPP, and TPP-BZ CMPs; their spherical diameters, evaluated statistically from the TEM images, were approximately 196, 246, 183, and 118 nm, respectively. The SEM and TEM results confirm that the synthesized CMPs have a porous structure.

Photophyscial Properties of CMPs. Maeda et al.[56,57] studied the fluorescence properties of the substituted pyrenes and employed them as fluorescence sensors. Hariharan et al.[58] reported the fluorescence efficiency of TPA and used it as an optoelectronic molecule. In addition, Schwarz and Wasik reported that the benzene unit provides fluorescence lower than that of the pyrene unit.[59] Also, Py and TPA are more electron enriched than TPP and BZ; therefore, we expected to observe various degrees of fluorescence from our CMPs. The solutions of the TPP-Py CMP in THF, dioxane, acetone, MeOH, and DMF featured their maximum fluorescence at 491, 497, 498, 500, and 490 nm, respectively (Figure 5a), as either a greenish-cyan or green color that was visible to the naked eye (Figure 5e). The fluorescence spectra of the TPP-TPA CMP solubilized in THF, dioxane, acetone, MeOH, and DMF provided fluorescence emission maxima at 487, 470, 506, 507, and, 518 nm, respectively, with a clear greenish-cyan or green color visible to the naked eye (Figure 5b,f), while the corresponding peaks for the TPP-TPP CMP were 410, 410, 410, 419, and 413 nm, respectively, appearing as a blue color visible to the naked eye (Figure 5c,g). Solutions of the TPP-BZ CMP in THF, dioxane, acetone, MeOH, and DMF displayed their maximum emissions at 449, 448, 458, 455, and 447 nm, respectively (Figure 5d), again appearing to the naked eye as a

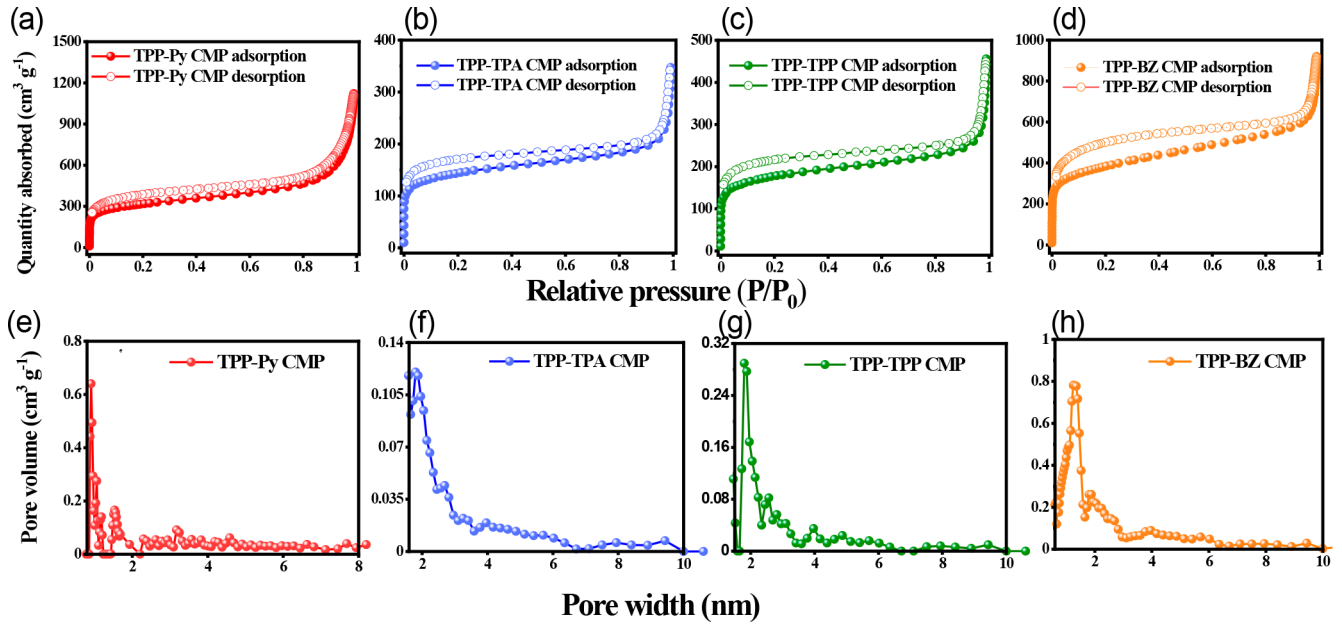

Figure 3. (a–d) N_2 sorption isotherms at 77 K and (e–h) pore size distributions of the TPP-Py, TPP-TPA, TPP-TPP, and TPP-BZ CMPs, respectively.

https://doi.org/10.1021/acsaem.1c02772
ACS Appl. Energy Mater. 2021, 4, 13140–13151

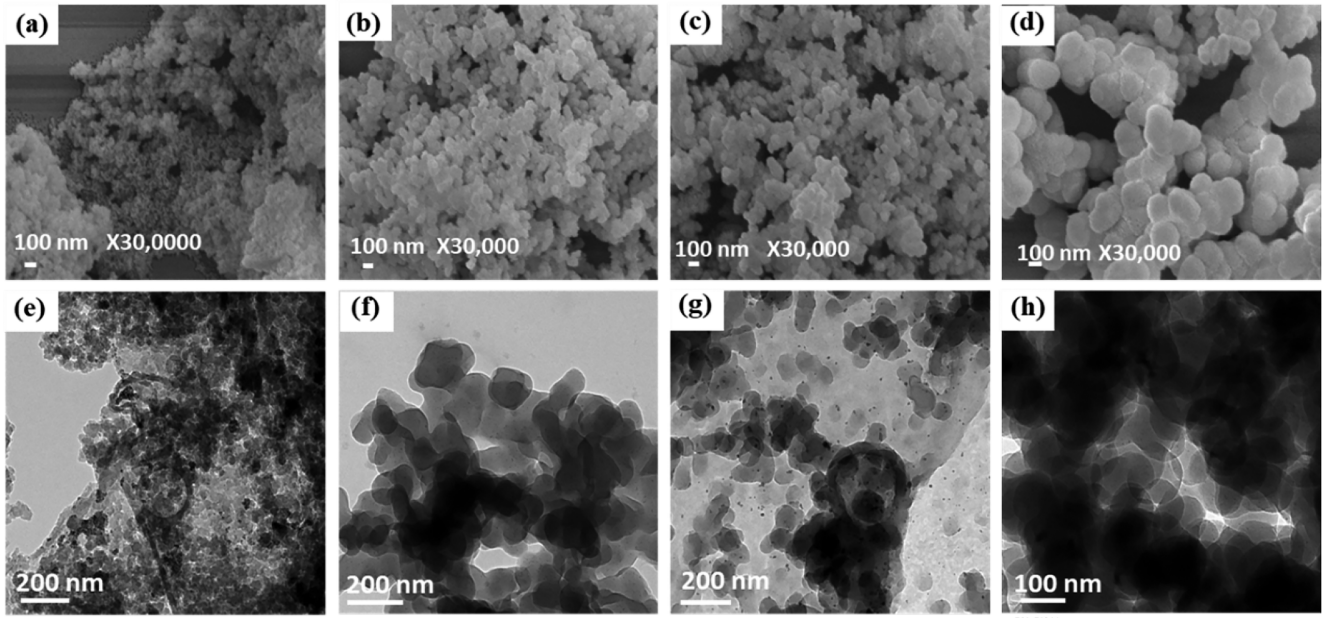

Figure 4. (a–d) FE-SEM and (e–h) TEM images of the (a, e) TPP-Py, (b, f) TPP-TPA, (c, g) TPP-TPP, and (d, h) TPP-BZ CMPs.

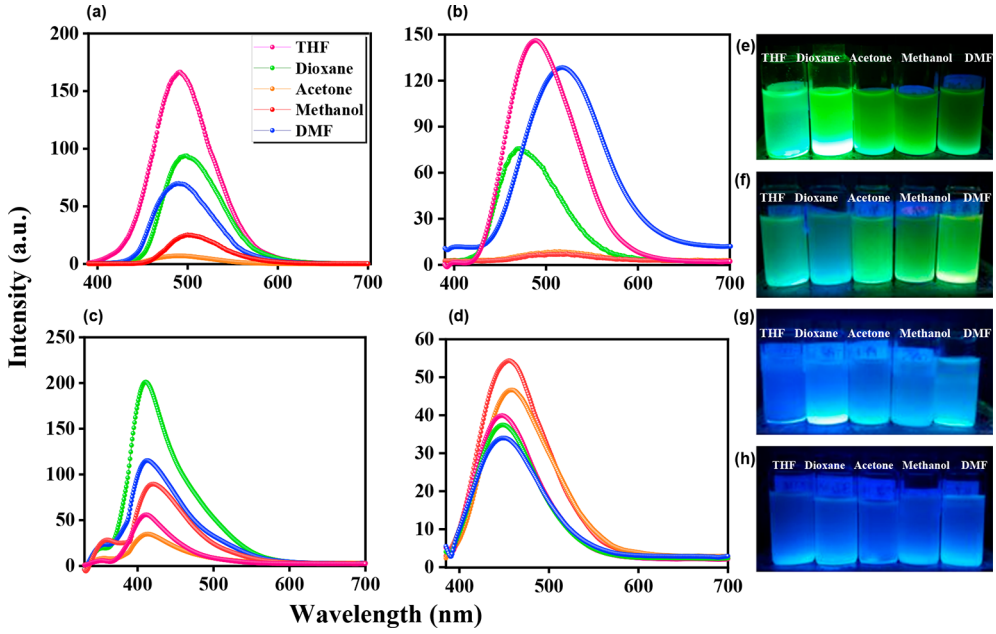

Figure 5. Fluorescence spectra of the (a) TPP-Py, (b) TPP-TPA, (c) TPP-TPP, and (d) TPP-BZ CMPs as dispersions in different solvents (concentration: 1 mg mL^{-1}; excitation wavelength: 365 nm). Photographic images of the (e) TPP-Py, (f) TPP-TPA, (g) TPP-TPP, and (h) TPP-BZ CMPs as dispersions in different solvents (concentration: 1 mg mL^{-1}; excitation wavelength: 365 nm).

blue color (Figure 5h). Thus, each of our four synthesized CMPs exhibited strong fluorescence (Table S1). A higher solvent polarity led to a higher wavenumber for the maximum emission (i.e., solvatochromism); this phenomenon can be characteristic of donor–π–acceptor moieties,[60] but an increase in the solvent polarity can also lead to a hypsochromic shift (negative solvatochromism) that reveals a higher dipole moment for the ground state than for the excited state.[61] Aggregation-induced emission (AIE) is typically observed for highly fluorescent materials in addition to emissions of various fluorescent colors; indeed, the TPP-Py and TPP-TPA CMPs displayed PL in the solid state with λ_{max} values of 505 and 468 nm, respectively (Figure S12a,b). These results are consistent with those reported previously;[58,59,62] we attribute the high AIE of the TPP-Py CMP to the high planarity and well-established stacking of its flat pyrene units,[63,64] but for the TPP-TPA CMP, we suspect that it was due to restricted intramolecular rotation (and, hence, activation as well as radiation).[65] The fluorescence lifetimes (Figure S13c–f) of the TPP-Py, TPP-TPA, TPP-TPP, and TPP-BZ CMPs were 3.45, 3.95, 4.96, and 5.12 ns, respectively. Our synthesized CMPs displayed high fluorescence stabilities with their fluorescence emissions remaining stable after keeping them in DMF for 60 days or after continuous excitation at 365 nm for 5 h.

Photocatalytic Hydrogen Evolution Efficacy of CMPs. Effective photocatalytic performance for a photocatalyst

https://doi.org/10.1021/acsaem.1c02772
ACS Appl. Energy Mater. 2021, 4, 13140–13151

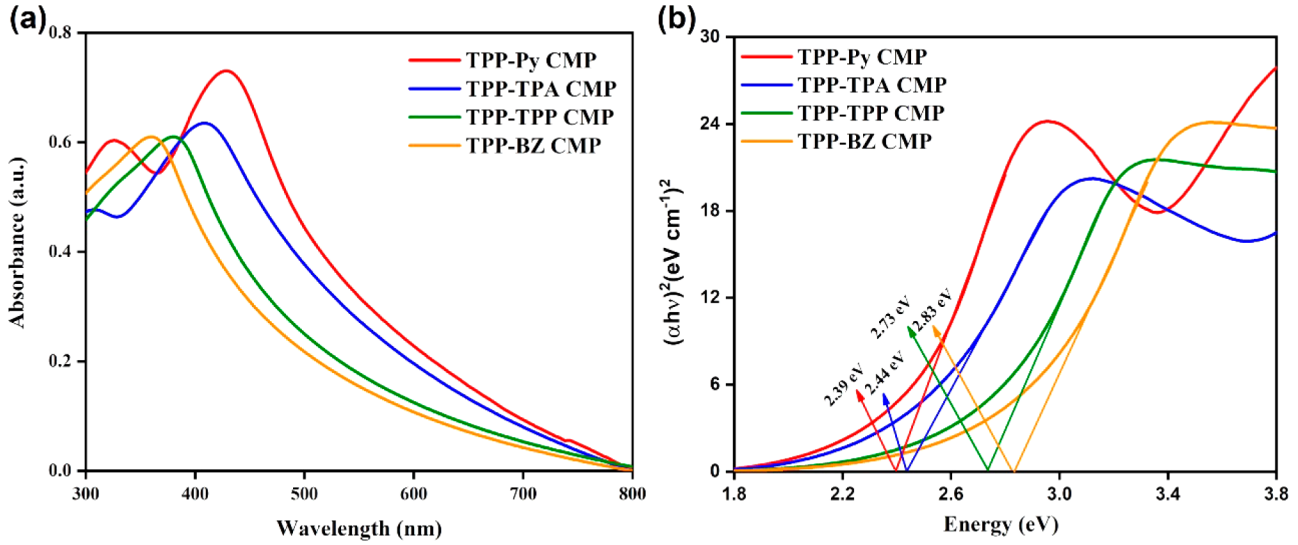

Figure 6. (a) UV−vis diffuse absorption spectra of the four CMPs and (b) corresponding Tauc plots calculated from the UV−vis spectra.

Table 2. Photophysical Properties and H_2 Evolution Rates of the Four CMPs

					AQY (%)[e]		
CMPs	HOMO/LUMO (eV)[a,b]	band gap (eV)[c]	HER (μmol g^{-1} h^{-1})[d]	HER (μmol h^{-1})	420 nm	460 nm	500 nm
TPP-Py CMP	−5.83/−3.44	2.39	18 065.6	18.06	22.9	11.8	0.50
TPP-TPA CMP	−5.68/−3.24	2.44	4827.7	4.827	7.60	2.50	0.09
TPP-TPP CMP	−5.06/−2.33	2.73	3583.6	3.583	0.90	0.17	0.02
TPP-BZ CMP	−5.16/−2.33	2.83	1518.6	1.518	0.57	0.07	0.01

[a]HOMO determined using photoelectron spectrometry. [b]LUMO derived from the expression $E_{HOMO} - E_g$. [c]Calculated from Tauc plots. [d]Conditions: 1 mg of CMP in 10 mL of a mixture of water/MeOH (2:1)/0.1 M AA, measured under 350 W Xe light (AM 1.5; λ = 380−780 nm; 1000 W m^{-2}). [e]AQYs measured at 420, 460, and 500 nm.

requires appropriate optical band gaps. Figure 6 shows UV−vis spectra and the corresponding band gaps of our four synthesized CMPs. We measured the UV−vis absorption spectra of these polymers in water at room temperature; all synthesized CMPs displayed a good absorption in the visible region (Figure 6a). As expected, the absorption band of TPP-Py CMP was a significant redshift relative to other polymers. The UV−visible reflectance spectra show a redshift in the optical absorption onset in the following order TPP-Py > TPP-TPA > TPP-TPP > TPP-BZ; this is because of its relatively extended π-conjugation and high electron enrichment. The optical band gaps of the TPP-Py, TPP-TPA, TPP-TPP, and TPP-BZ CMPs, calculated from their absorption spectra using Tauc plots, were 2.39, 2.44, 2.73, and 2.83 eV, respectively (Figure 6b, Table 2). Photoelectron spectrophotometry was used to determine the energy levels of the highest occupied molecular orbitals (HOMOs) of the TPP-Py, TPP-TPA, TPP-TPP, and TPP-BZ CMPs to be −5.83, −5.68, −5.06, and −5.16 eV, respectively (Figures 7a and S14). We calculated the energy levels of the lowest unoccupied molecular orbitals (LUMOs) by subtracting the values of E_g from the HOMO energy levels. As revealed in Figure 7a and Table 2, the LUMO energy levels of the CMPs ranged from −2.33 to −3.44 eV, suggesting that all polymers would be capable of visible light-driven H_2 evolution.

We employed TPP-Py, TPP-TPA, TPP-TPP, and TPP-BZ CMPs photocatalysts for hydrogen production under irradiation with visible light (λ = 380−780 nm) at ambient temperature for 4 h. The photocatalytic systems were designed by adding ascorbic acid (AA, 0.1M) as a sacrificial electron donor (SED) to a CMP with water and methanol in a glass photoreactor (35 mL). The evolved gas (500 μL) from the photoreactor was monitored periodically every hour and injected into a gas chromatograph (GC). First, we employed triethylamine (TEA), triethanolamine (TEOA), and ascorbic acid (AA) to optimize the sacrificial donors. Among them, AA shows the highest efficient SED as compared to those of TEA and TEOA (Figures S15−S18). As shown in Figure 7b, the TPP-Py CMP exhibited the highest photocatalytic performance (ca. 18 100 μmol g^{-1} h^{-1}); the HERs of the TPP-TPA, TPP-TPP, and TPP-BZ CMPs were 4830, 3580, and 1520 μmol g^{-1} h^{-1}, respectively. Therefore, AA was used after that to optimize the other experiments. Also, the concentrations of AA have been optimized as shown in Figures S19−S22.

Next, we examined the effects of various contents of Pt as a cocatalyst (source of Pt is H_2PtCl_6: 0.5−4 wt %) for the polymers when applying their optimal experimental parameters for H_2 evolution (Figures S23 and S24). Remarkably, 2 wt % of Pt noble metal as a cocatalyst added into the polymer solution exhibited an excellent HER. We also tested the effects of different amounts (0.5, 1.0, 1.5, 3.0 mg) of our four synthesized CMPs toward the HERs (Figures S25−S28). The photocatalytic activity is inversely proportional to the mass of the polymers. The amount of hydrogen produced per unit area irradiated is the most important parameter in the field of photocatalysis. As shown in Figure S25, the best performance of 23.5 mmol g^{-1} h^{-1} was for TPP-Py CMP at 0.5 mg, but the best performances for other polymers have been achieved when using 1 mg catalysts. With an increase in the amount of polymer, the HER decreased, which can be

https://doi.org/10.1021/acsaem.1c02772
ACS Appl. Energy Mater. 2021, 4, 13140−13151

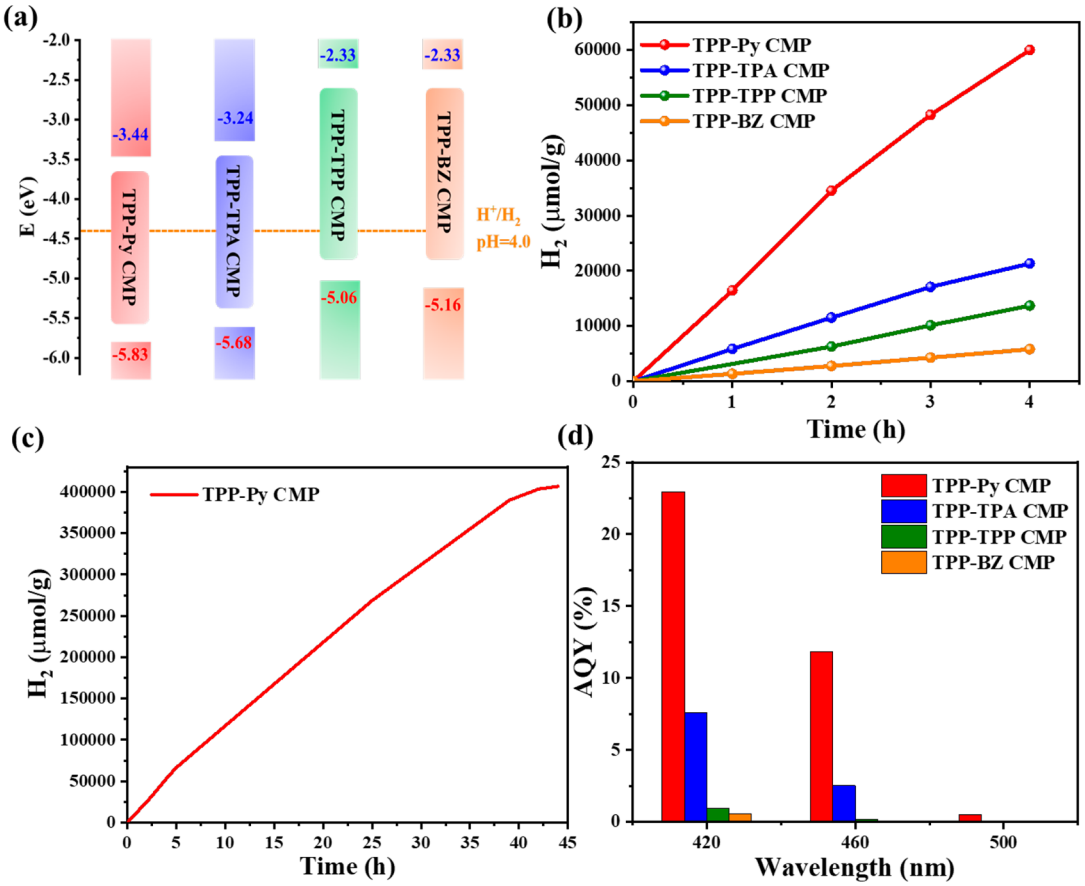

Figure 7. (a) Electronic band structures of the CMPs; orange line: redox potential of H^+/H_2. (b) H_2 evolution under irradiation with visible light (λ = 380−780 nm) mediated by the TPP-based CMPs. (c) Photocatalytic stability of TPP-Py CMP. (d) Wavelength dependence of the AQY of the H_2 evolution mediated by the CMPs.

attributed to the poor light transmission and less effective use of the high concentrations of light. Herein, a polymer weight of 1 mg has been selected for all polymers. After optimization, the H_2 evolution rates of the four polymers are shown in Figure 7b. Among them, the TPP-Py CMP shows the highest HER value (18.1 mmol g^{-1} h^{-1}) compared to those of TPP-TPA CMP (4.8 mmol g^{-1} h^{-1}) and TPP-TPP CMP (3.6 mmol g^{-1} h^{-1}), and it is even 12-fold higher than that of TPP-BZ CMP (1.8 mmol g^{-1} h^{-1}). This result is well consistent with the UV−vis data. The higher HER of TPP-Py CMP is attributed to the narrow bandgap, which in turn improves the light-harvesting ability to produce sufficient charge carriers. In addition, the increased planarity in TPP-Py CMP gives lower degrees of torsion, which increases the intramolecular charge transfer along the polymer backbone, given that conjugated network polymers with greater adjacent unit planarity have improved intramolecular charge transfer.[66] The photocatalytic performance of our CMPs, especially TPP-Py CMP, is higher than that of several recently reported CMPs, as reported in Table S2. Most importantly, the TPP-Py CMP not only enhances the hydrogen production rate but also leads to an increase in the photocatalytic stability under continuous irradiation for ∼40 h as shown in Figure 7c; additionally, recycling experiments were conducted as shown in Figures S29−S32, in which TPP-Py CMP represents a good photocatalytic stability, which can maintain the HER in more than five cycles without loss in the photocatalytic efficiency (Figure S29). The apparent quantum yield (AQY) of these polymers is calculated under the optimized conditions at 420, 460, and 500 nm using monochromatic light (Figure 7d). As shown, the AQY was decreased with an increase in the wavelength. These results are in a good agreement with the trend observed in the absorption spectra. Notably, TPP-Py CMP showed a higher AQY value of 22.97% at 420 nm compared to that of the other polymers. The high AQY of the TPP-Py CMP (22.97% at 420 nm) rivals those of most of the CMPs reported previously. The photoluminescence (PL) is closely related to the recombination of photoexcited electron−hole pairs. In general, lower PL intensity results in a higher degree of charge separation.[67] Figure 8a presents the PL spectra of the CMPs. Notably, the TPP-Py CMP exhibited the lowest PL intensity, indicating that the recombination of electrons and holes was effectively suppressed relative to that of the other polymers. The PL intensities decreased in the order TPP-Py CMP < TPP-TPA CMP < TPP-TPP CMP < TPP-TPB CMP, consistent with the photocatalytic efficiencies. To gain insight into the intramolecular charge transfer characteristics of the CMPs, we examined their photocurrents (Figure 8b). The TPP-Py CMP provided the highest photocurrent among our CMPs; the photocurrents followed the order TPP-Py CMP > TPP-TPA CMP > TPP-TPP CMP > TPP-TPB CMP.

The photocurrent data revealed the possibility of separation, in addition to transfer, of photogenerated electrons induced upon illumination of the CMPs; this process was most evident for the TPP-Py CMP. We used electrochemical impedance spectroscopy (EIS) to examine the accelerated charge transfer.

https://doi.org/10.1021/acsaem.1c02772
ACS Appl. Energy Mater. 2021, 4, 13140−13151

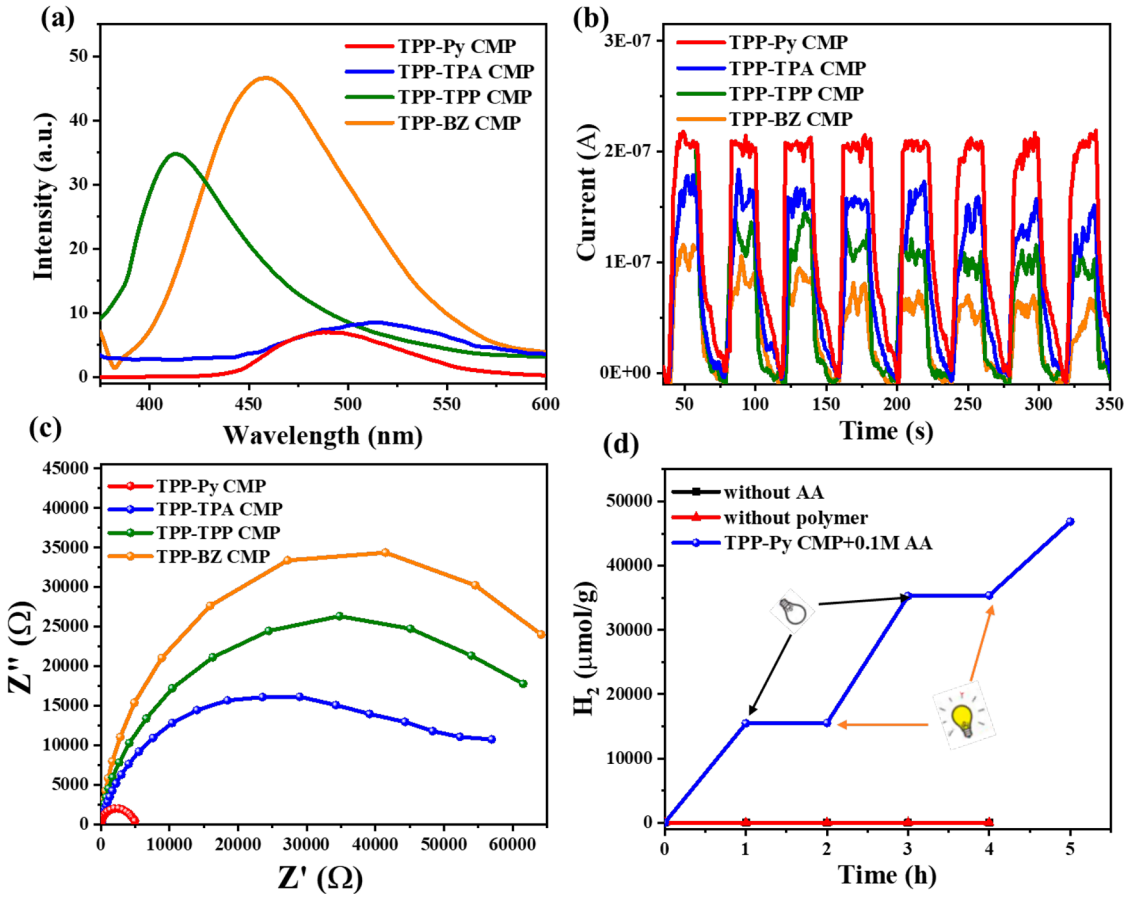

Figure 8. (a) PL emission spectra of the CMPs in acetone; excitation wavelength: 365 nm. (b) Photocurrent responses and (c) EIS of the CMPs under irradiation with visible light (LED lamp; λ > 420 nm). (d) Control experiment of the TPP-Py CMPs.

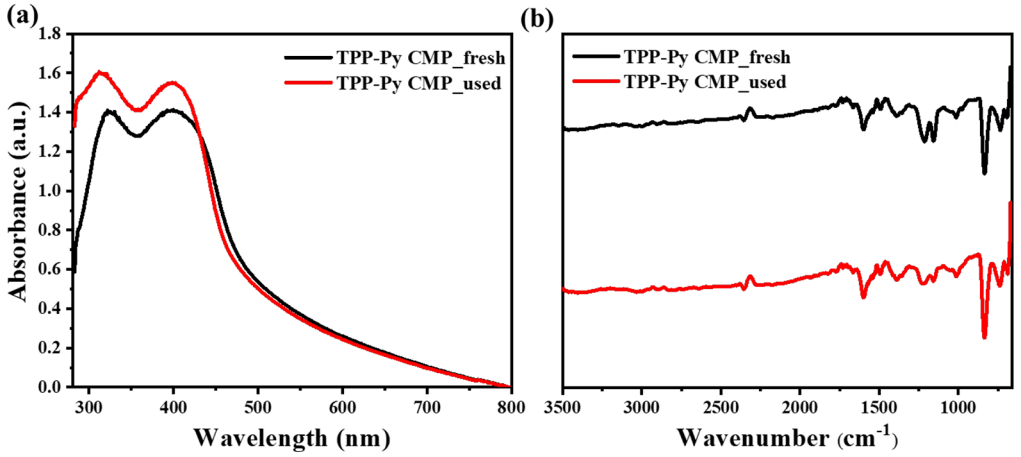

Figure 9. (a) UV−vis absorption and (b) FTIR spectra of the TPP-Py CMP photocatalyst before and after the photoreaction.

Figure 8c reveals that the TPP-Py CMP provided a lower-intensity EIS spectrum relative to those of the other CMPs, which indicates a smaller charge resistance in TPP-Py CMP.

This result strongly agrees with the HER activity. Next, DFT calculations were performed at the B3LYP level with the 6-31G(d,p) basis set to elucidate the structure−property relationship of these four polymers and HOMO/LUMO separations (Figures S33−S36). The results show that the HOMO is mainly localized on Py, TPA, TPP, and BZ, indicating that this group acts as a donor. These results show that the donor group (Py, TPA, TPP, and BZ) conjugation can effectively expand the delocalization of the HOMO levels, which might facilitate the charge transport to ensure their high mobility. Finally, the control experiments performed at ambient temperature revealed that the photocatalytic process was increased under a light-on condition and decreased under a light-off condition, confirming that our system was a photocatalytic reaction as well as had nondetectable reactions in the absence of the photocatalysts or electron donor molecules (e.g., AA) (Figures 8d and S37−S39).

The stability of the photocatalyst is an important factor affecting its applicability. Accordingly, we investigated the

https://doi.org/10.1021/acsaem.1c02772
ACS Appl. Energy Mater. 2021, 4, 13140−13151

stability of our CMPs during photocatalytic H_2 production (Figures 9 and S40). The UV−vis and FTIR spectra of these CMPs recorded before and after the photocatalytic reaction revealed no apparent changes. The results clearly reveal the good structural stability of our polymers.

CONCLUSION

We have synthesized and characterized a series of pyridine-based CMPs for use as photocatalysts for the photocatalytic production of H_2 from water under irradiation with visible light. The optical properties of the CMPs revealed that variations in the structure of their monomers could be used to systematically tune the resulting optical gap over a broad range (2.39−2.83 eV), depending on their electron rich or poor counterparts. The most highly planar CMP having the highest electron enrichment CMP (TPP-Py CMP) and the narrowest band gap provided excellent H_2 evolution rates (up to 18 100 μmol g^{-1} h^{-1}) and a high AQY of 22.97% at 420 nm. This modular approach for the synthesis of CMPs provides the opportunity to tune their photocatalytic and porous properties that determine their suitability for use as organic photocatalysts.

ASSOCIATED CONTENT

Supporting Information

The Supporting Information is available free of charge at https://pubs.acs.org/doi/10.1021/acsaem.1c02772.

Characterization techniques, synthetic schemes, detailed FTIR profiles, ^{1}H and ^{13}C NMR profiles, mass spectroscopy profile, TGA analysis, BET parameters, florescence parameters, HOMO parameters, additional photocatalytic hydrogen evolution analysis, and comparative studies (PDF)

AUTHOR INFORMATION

Corresponding Authors

Ahmed F. M. EL-Mahdy − *Department of Materials and Optoelectronic Science, Center for Functional Polymer and Supramolecular Materials, National Sun Yat-Sen University, Kaohsiung 80424, Taiwan;* orcid.org/0000-0002-5237-750X; Email: ahmedelmahdy@mail.nsysu.edu.tw

Ho-Hsiu Chou − *Department of Chemical Engineering, National Tsing Hua University, Hsinchu 30013, Taiwan;* orcid.org/0000-0003-3777-2277; Email: hhchou@mx.nthu.edu.tw

Shiao-Wei Kuo − *Department of Materials and Optoelectronic Science, Center for Functional Polymer and Supramolecular Materials, National Sun Yat-Sen University, Kaohsiung 80424, Taiwan; Department of Medicinal and Applied Chemistry, Kaohsiung Medical University, Kaohsiung 807, Taiwan;* orcid.org/0000-0002-4306-7171; Email: kuosw@faculty.nsysu.edu.tw

Authors

Mohammed G. Kotp − *Department of Materials and Optoelectronic Science, Center for Functional Polymer and Supramolecular Materials, National Sun Yat-Sen University, Kaohsiung 80424, Taiwan*

Ahmed M. Elewa − *Department of Chemical Engineering, National Tsing Hua University, Hsinchu 30013, Taiwan;* orcid.org/0000-0001-8943-5710

Complete contact information is available at: https://pubs.acs.org/10.1021/acsaem.1c02772

Author Contributions

$^{\nabla}$M.G.K. and A.M.E. contributed equally.

Notes

The authors declare no competing financial interest.

ACKNOWLEDGMENTS

We thank the Ministry of Science and Technology of Taiwan for financial support (MOST 108-2218-E-110-013-MY3, MOST 110-2636-E-007-020, and MOST 110-2622-8-007-015), the National Center for High-Performance Computing of Taiwan for providing the computing time, and the Precision Instrument Support Center of National Tsing Hua University for providing the analysis and measurement facilities.

REFERENCES

(1) Jayakumar, J.; Chou, H. H. Recent Advances in Visible-Light-Driven Hydrogen Evolution from Water using Polymer Photocatalysts. *ChemCatChem* **2020**, *12*, 689−704.

(2) Yu, J.; Sun, X.; Xu, X.; Zhang, C.; He, X. Donor-acceptor type triazine-based conjugated porous polymer for visible-light-driven photocatalytic hydrogen evolution. *Appl. Catal., B* **2019**, *257*, 117935.

(3) Fujishima, A. A.; Honda, K. Electrochemical photolysis of water at a semiconductor electrode. *Nature* **1972**, *238*, 37−38.

(4) Zhang, Q.; Xiao, Y.; Li, Y.; Zhao, K.; Deng, H.; Lou, Y.; Chen, J.; Cheng, L. NiS-Decorated ZnO/ZnS Nanorod Heterostructures for Enhanced Photocatalytic Hydrogen Production: Insight into the Role of NiS. *Sol. RRL* **2020**, *4*, 1900568.

(5) Liu, C.; Li, J.; Sun, L.; Zhou, Y.; Liu, C.; Wang, H.; Huo, P.; Ma, C.; Yan, Y. Visible-light driven photocatalyst of CdTe/CdS homologous heterojunction on N-rGO photocatalyst for efficient degradation of 2, 4-dichlorophenol. *J. Taiwan Inst. Chem. Eng.* **2018**, *93*, 603−615.

(6) Jiang, C.; Zhang, L.; Gao, F.; Huang, X.; Lei, R.; Ye, Y.; Yuan, J.; Liu, P. Promoting photocatalytic hydrogen production by a core−shell CdS@ MoO x photocatalyst connected by an S−Mo "bridge. *Catal. Sci. Technol.* **2020**, *10*, 1368−1375.

(7) Wang, X.; Maeda, K.; Thomas, A.; Takanabe, K.; Xin, G.; Carlsson, J. M.; Domen, K.; Antonietti, M. A metal-free polymeric photocatalyst for hydrogen production from water under visible light. *Nat. Mater.* **2009**, *8*, 76−80.

(8) Elewa, A. M.; Elsayed, M. H.; EL-Mahdy, A. F. M.; Chang, C.-L.; Ting, L.-Y.; Lin, W.-C.; Lu, C.-Y.; Chou, H.-H. Triptycene-based discontinuously-conjugated covalent organic polymer photocatalysts for visible-light-driven hydrogen evolution from water. *Appl. Catal., B* **2021**, *285*, 119802.

(9) Wang, W.-H.; Ting, L.-Y.; Jayakumar, J.; Chang, C.-L.; Lin, W.-C.; Chung, C.-C.; Elsayed, M. H.; Lu, C.-Y.; Elewa, A. M.; Chou, H.-H. Design and synthesis of phenylphosphine oxide-based polymer photocatalysts for highly efficient visible-light-driven hydrogen evolution. *Sustain. Energy Fuels* **2020**, *4*, 5264−5270.

(10) Lin, W.-C.; Elsayed, M. H.; Jayakumar, J.; Ting, L.-Y.; Chang, C.-L.; Elewa, A. M.; Wang, W.-S.; Chung, C.-C.; Lu, C.-Y.; Chou, H.-H. Design and synthesis of cyclometalated iridium-based polymer dots as photocatalysts for visible light-driven hydrogen evolution. *Int. J. Hydrogen Energy* **2020**, *45*, 32072−32081.

(11) Ting, L.-Y.; Jayakumar, J.; Chang, C.-L.; Lin, W.-C.; Elsayed, M. H.; Chou, H.-H. Effect of controlling the number of fused rings on polymer photocatalysts for visible-light-driven hydrogen evolution. *J. Mater. Chem. A* **2019**, *7*, 22924−22929.

(12) Zhao, X.; Zhang, X.; Liang, Y.; Hu, Z.; Huang, F. Porphyrin-Based Conjugated Polyelectrolytes for Efficient Photocatalytic Hydrogen Evolution. *Macromolecules* **2021**, *54*, 4902−4909.

(13) Tseng, P.-J.; Chang, C.-L.; Chan, Y.-H.; Ting, L.-Y.; Chen, P.-Y.; Liao, C.-H.; Tsai, M.-L.; Chou, H.-H. Design and Synthesis of

Cycloplatinated Polymer Dots as Photocatalysts for Visible-Light-Driven Hydrogen Evolution. *ACS Catal.* **2018**, *8*, 7766−7772.
(14) Chang, C.-L.; Lin, W.-C.; Jia, C.-Y.; Ting, L.-Y.; Jayakumar, J.; Elsayed, M. H.; Yang, Y.-Q.; Chan, Y.-H.; Wang, W.-S.; Lu, C.-Y. Low-toxic cycloplatinated polymer dots with rational design of acceptor co-monomers for enhanced photocatalytic efficiency and stability. *Appl. Catal., B* **2020**, *268*, 118436.
(15) Elsayed, M. H.; Jayakumar, J.; Abdellah, M.; Mansoure, T. H.; Zheng, K.; Elewa, A. M.; Chang, C.-L.; Ting, L.-Y.; Lin, W.-C.; Yu, H.-H. Visible-light-driven hydrogen evolution using nitrogen-doped carbon quantum dot-implanted polymer dots as metal-free photocatalysts. *Appl. Catal., B* **2021**, *283*, 119659.
(16) Zhao, P.; Wang, L.; Wu, Y.; Yang, T.; Ding, Y.; Yang, H. G.; Hu, A. Hyperbranched Conjugated Polymer Dots: The Enhanced Photocatalytic Activity for Visible Light-Driven Hydrogen Production. *Macromolecules* **2019**, *52*, 4376−4384.
(17) Bai, Y.; Hu, Z.; Jiang, J. X.; Huang, F. Hydrophilic Conjugated Materials for Photocatalytic Hydrogen Evolution. *Chem. - Asian J.* **2020**, *15*, 1780−1790.
(18) Wang, J.; Feng, K.; Chen, B.; Li, Z.-J.; Meng, Q.-Y.; Zhang, L.-P.; Tung, C.-H.; Wu, L.-Z. Polymer-modified hydrophilic graphene: A promotor to photocatalytic hydrogen evolution for in situ formation of core@ shell cobalt nanocomposites. *J. Photochem. Photobiol., A* **2016**, *331*, 247−254.
(19) Wang, J. L.; Ouyang, G.; Wang, D.; Li, J.; Yao, J.; Li, W. S.; Li, H. Enhanced Photocatalytic Performance of Donor−Acceptor-Type Polymers Based on a Thiophene-Contained Polycyclic Aromatic Unit. *Macromolecules* **2021**, *54*, 2661−2666.
(20) Cheng, Z.; Fang, W.; Zhao, T.; Fang, S.; Bi, J.; Liang, S.; Li, L.; Yu, Y.; Wu, L. Efficient visible-light-driven photocatalytic hydrogen evolution on phosphorus-doped covalent triazine-based frameworks. *ACS Appl. Mater. Interfaces* **2018**, *10*, 41415−41421.
(21) Xu, T.; Li, Y.; Zhao, Z.; Xing, G.; Chen, L. *N,N′*-Bicarbazole-Based Covalent Triazine Frameworks as High-Performance Heterogeneous Photocatalysts. *Macromolecules* **2019**, *52*, 9786−9791.
(22) EL-Mahdy, A. F. M.; Elewa, A. M.; Huang, S. W.; Chou, H. H.; Kuo, S. W. Dual-Function Fluorescent Covalent Organic Frameworks: HCl Sensing and Photocatalytic H2 Evolution from Water. *Adv. Opt. Mater.* **2020**, *8*, 2000641.
(23) Pachfule, P.; Acharjya, A.; Roeser, J.; Langenhahn, T.; Schwarze, M.; Schomäcker, R.; Thomas, A.; Schmidt, J. Diacetylene Functionalized Covalent Organic Framework (COF) for Photocatalytic Hydrogen Generation. *J. Am. Chem. Soc.* **2018**, *140*, 1423−1427.
(24) Xu, N.; Liu, Y.; Yang, W.; Tang, J.; Cai, B.; Li, Q.; Sun, J.; Wang, K.; Xu, B.; Zhang, Q.; Fan, Y. 2D−2D Heterojunctions of a Covalent Triazine Framework with a Triphenylphosphine-Based Covalent Organic Framework for Efficient Photocatalytic Hydrogen Evolution. *ACS Appl. Energy Mater.* **2020**, *3*, 11939−11946.
(25) EL-Mahdy, A. F. M.; Zakaria, M. B.; Wang, H.-X.; Chen, T.; Yamauchi, Y.; Kuo, S.-W. Heteroporous bifluorenylidene-based covalent organic frameworks displaying exceptional dye adsorption behavior and high energy storage. *J. Mater. Chem. A* **2020**, *8*, 25148−25155.
(26) EL-Mahdy, A. F. M.; Kuo, C.-H.; Alshehri, A.; Young, C.; Yamauchi, Y.; Kim, J.; Kuo, S.-W. Strategic design of triphenylamine- and triphenyltriazine-based two-dimensional covalent organic frameworks for CO_2 uptake and energy storage. *J. Mater. Chem. A* **2018**, *6*, 19532−19541.
(27) Mohamed, M. G.; Elsayed, M. H.; Elewa, A. M.; EL-Mahdy, A. F. M.; Yang, C.-H.; Mohammed, A. A.; Chou, H.-H.; Kuo, S.-W. Pyrene-containing conjugated organic microporous polymers for photocatalytic hydrogen evolution from water. *Catal. Sci. Technol.* **2021**, *11*, 2229−2241.
(28) Gao, X.; Shu, C.; Zhang, C.; Ma, W.; Ren, S.-B.; Wang, F.; Chen, Y.; Zeng, J. H.; Jiang, J.-X. Substituent effect of conjugated microporous polymers on the photocatalytic hydrogen evolution activity. *J. Mater. Chem. A* **2020**, *8*, 2404−2411.
(29) Elewa, A. M.; EL-Mahdy, A. F. M.; Elsayed, M. H.; Mohamed, M. G.; Kuo, S. W.; Chou, H. H. Sulfur-doped triazine-conjugated microporous polymers for achieving the robust visible-light-driven hydrogen evolution. *Chem. Eng. J.* **2021**, *421*, 129825.
(30) Abuzeid, H. R.; EL-Mahdy, A. F. M.; Kuo, S. W. Hydrogen bonding induces dual porous types with microporous and mesoporous covalent organic frameworks based on bicarbazole units. *Microporous Mesoporous Mater.* **2020**, *300*, 110151.
(31) Jiang, J. X.; Su, F.; Trewin, A.; Wood, C. D.; Campbell, N. L.; Niu, H.; Dickinson, C.; Ganin, A. Y.; Rosseinsky, M. J.; Khimyak, Y. Z. Conjugated microporous poly (aryleneethynylene) networks. *Angew. Chem., Int. Ed.* **2007**, *46*, 8574−8578.
(32) Nailwal, Y.; Dinga Wonanke, A. D.; Addicoat, M. A.; Pal, S. K. A Dual-Function Highly Crystalline Covalent Organic Framework for HCl Sensing and Visible-Light Heterogeneous Photocatalysis. *Macromolecules* **2021**, *54*, 6595−6604.
(33) EL-Mahdy, A. F. M; Lüder, J.; Kotp, M. G.; Kuo, S. W. A Tröger's base-derived covalent organic polymer containing carbazole units as a high-performance supercapacitor. *Polymers* **2021**, *13*, 1385.
(34) Xiao, W. J.; Wang, Y.; Wang, W. R.; Li, J.; Wang, J.; Xu, Z. W.; Li, J.; Yao, J.; Li, W. S. Diketopyrrolopyrrole-Based Donor-Acceptor Conjugated Microporous Polymers for Visible-Light-Driven Photocatalytic Hydrogen Production from Water. *Macromolecules* **2020**, *53*, 2454−2463.
(35) Xu, Y.; Jin, S.; Xu, H.; Nagai, A.; Jiang, D. Conjugated microporous polymers: design, synthesis and application. *Chem. Soc. Rev.* **2013**, *42*, 8012−8031.
(36) Li, H.; Lyu, W.; Liao, Y. Engineering Redox Activity in Conjugated Microporous Polytriphenylamine Networks Using Pyridyl Building Blocks toward Efficient Supercapacitors. *Macromol. Rapid Commun.* **2019**, *40*, 1900455.
(37) El-Mahdy, A. F. M.; Young, C.; Kim, J.; You, J.; Yamauchi, Y.; Kuo, S. W. Hollow Microspherical and Microtubular [3+ 3] Carbazole-Based Covalent Organic Frameworks and Their Gas and Energy Storage Applications. *ACS Appl. Mater. Interfaces* **2019**, *11*, 9343−9354.
(38) Mohamed, M. G.; Atayde, E. C.; Matsagar, B. M.; Na, J.; Yamauchi, Y.; Wu, K. C. W.; Kuo, S. W. Construction Hierarchically Mesoporous/Microporous Materials Based on Block Copolymer and Covalent Organic Framework. *J. Taiwan Inst. Chem. Eng.* **2020**, *112*, 180.
(39) Abuzeid, H. R.; EL-Mahdy, A. F. M.; Kuo, S. W. Covalent Organic Frameworks: Design Principles, Synthetic Strategies, and Diverse Applications. *Giant* **2021**, *6*, 100054.
(40) Wang, H.; Hou, B.; Yang, Y.; Chen, Q.; Zhu, M.; Thomas, A.; Liao, Y. Cobalt Nanocrystals Encapsulated in Heteroatom-Rich Porous Carbons Derived from Conjugated Microporous Polymers for Efficient Electrocatalytic Hydrogen Evolution. *Small* **2018**, *14*, 1803232.
(41) Dai, C.; Xu, S.; Liu, W.; Gong, X.; Panahandeh-Fard, M.; Liu, Z.; Zhang, D.; Xue, C.; Loh, K. P.; Liu, B. Dibenzothiophene-S, S-Dioxide-Based Conjugated Polymers: Highly Efficient Photocatalyts for Hydrogen Production from Water under Visible Light. *Small* **2018**, *14*, 1801839.
(42) Sprick, R. S.; Jiang, J.-X.; Bonillo, B.; Ren, S.; Ratvijitvech, T.; Guiglion, P.; Zwijnenburg, M. A.; Adams, D. J.; Cooper, A. I. Tunable organic photocatalysts for visible-light-driven hydrogen evolution. *J. Am. Chem. Soc.* **2015**, *137*, 3265−3270.
(43) Sprick, R. S.; Bai, Y.; Guilbert, A. A.; Zbiri, M. C.; Aitchison, M.; Wilbraham, L.; Yan, Y.; Woods, D. J.; Zwijnenburg, M. A.; Cooper, A. I. Photocatalytic hydrogen evolution from water using fluorene and dibenzothiophene sulfone-conjugated microporous and linear polymers. *Chem. Mater.* **2019**, *31*, 305−313.
(44) Tamami, B.; Yeganeh, H. Preparation and properties of novel polyimides derived from 4-aryl-2, 6 bis (4-amino phenyl) pyridine. *J. Polym. Sci., Part A: Polym. Chem.* **2001**, *39*, 3826−3831.
(45) Kanbara, T.; Saito, N.; Yamamoto, T.; Kubota, K. Preparation and properties of poly (quinolinediyl) s and poly (isoquinoline-1, 4-

https://doi.org/10.1021/acsaem.1c02772
ACS Appl. Energy Mater. 2021, 4, 13140−13151

diyl) with new π-conjugation systems. *Macromolecules* **1991**, *24*, 5883−5885.
(46) Dailey, S.; Halim, M.; Rebourt, E.; Horsburgh, L.; Samuel, I.; Monkman, A. An efficient electron-transporting polymer for light-emitting diodes. *J. Phys.: Condens. Matter* **1998**, *10*, 5171.
(47) Bai, Q.; Liu, H.; Yao, L.; Shan, T.; Li, J.; Gao, Y.; Zhang, Z.; Liu, Y.; Lu, P.; Yang, B. Adjusting nitrogen atom orientations of pyridine ring in tetraphenylsilane-based hosts for highly efficient blue phosphorescent organic light-emitting devices. *ACS Appl. Mater. Interfaces* **2016**, *8*, 24793−24802.
(48) Costuas, K.; Cador, O.; Justaud, F.; Le Stang, S.; Paul, F.; Monari, A.; Evangelisti, S.; Toupet, L.; Lapinte, C.; Halet, J.-F. 3, 5-Bis (ethynyl) pyridine and 2, 6-bis (ethynyl) pyridine spanning two Fe (Cp*)(dppe) units: role of the nitrogen atom on the electronic and magnetic couplings. *Inorg. Chem.* **2011**, *50*, 12601−12622.
(49) Cheng, Z.; Wang, L.; He, Y.; Chen, X.; Wu, X.; Xu, H.; Liao, Y.; Zhu, M. Rapid metal-free synthesis of pyridyl-functionalized conjugated microporous polymers for visible-light-driven water splitting. *Polym. Chem.* **2020**, *11*, 3393−3397.
(50) Najare, M. S.; Patil, M. K.; Nadaf, A. A.; Mantur, S.; Inamdar, S. R.; Khazi, I. A. M. Synthesis, characterization and photophysical properties of a new class of pyrene substituted 1, 3, 4-oxadiazole derivatives. *Opt. Mater.* **2019**, *88*, 256−265.
(51) Wang, P.-I.; Shie, W.-R.; Jiang, J.-C.; Li, L.-J.; Liaw, D.-J. Novel poly (triphenylamine-alt-fluorene) with asymmetric hexaphenylbenzene and pyrene moieties: synthesis, fluorescence, flexible near-infrared electrochromic devices and theoretical investigation. *Polym. Chem.* **2016**, *7*, 1505−1516.
(52) Ran, Q.; Ma, J.; Wang, T.; Fan, S.; Yang, Y.; Qi, S.; Cheng, Y.; Song, F. Synthesis and fluorescence study of conjugated polymers based on 2, 4, 6-triphenylpyridine moieties. *New J. Chem.* **2016**, *40*, 6281−6288.
(53) Rodríguez-Seco, C.; MéNdez, M.; RoldáN-Carmona, C.; Cabau, L.; Asiri, A. M.; Nazeeruddin, M. K.; Palomares, E. Benzothiadiazole Aryl-amine Based Materials as Efficient Hole Carriers in Perovskite Solar Cells. *ACS Appl. Mater. Interfaces* **2020**, *12*, 32712−32718.
(54) Geng, T.; Ma, L.; Chen, G.; Zhang, C.; Zhang, W.; Niu, Q. Fluorescent conjugated microporous polymers containing pyrazine moieties for adsorbing and fluorescent sensing of iodine. *Environ. Sci. Pollut. Res.* **2020**, *27*, 20235−20245.
(55) Wang, P.-I.; Shie, W.-R.; Jiang, J.-C.; Li, L.-J.; Liaw, D.-J. Novel poly (triphenylamine-alt-fluorene) with asymmetric hexaphenylbenzene and pyrene moieties: synthesis, fluorescence, flexible near-infrared electrochromic devices and theoretical investigation. *Polym. Chem.* **2016**, *7*, 1505−1516.
(56) Maeda, H.; Suzuki, T.; Segi, M. Effects of substituents in silyl groups on the absorption, fluorescence and structural properties of 1, 3, 6, 8-tetrasilylpyrenes. *Photochem. Photobiol. Sci.* **2018**, *17*, 781−792.
(57) Maeda, H.; Nakamura, K.; Furuyama, T.; Segi, M. (1, 3) Pyrenophanes containing crown ether moieties as fluorescence sensors for metal and ammonium ions, *Photochem. Photobiol. Sci.* **2019**, *18*, 2397−2410.
(58) Hariharan, P. S.; Prasad, V. K.; Nandi, S.; Anoop, A.; Moon, D.; Anthony, S. P. Molecular engineering of triphenylamine based aggregation enhanced emissive fluorophore: structure-dependent mechanochromism and self-reversible fluorescence switching. *Cryst. Growth Des.* **2017**, *17*, 146−155.
(59) Schwarz, F. P.; Wasik, S. P. Fluorescence measurements of benzene, naphthalene, anthracene, pyrene, fluoranthene, and benzo [e] pyrene in water. *Anal. Chem.* **1976**, *48*, 524−528.
(60) Islam, A.; Zhang, D.; Hong, L.; Cui, H.; Wei, Q.; Duan, L.; Peng, R.; Ouyang, X.; Ge, Z. Efficient deep blue emitter based on the integration of phenanthroimidazole, triphenylamine and tetraphenylethene for organic light emitting devices. *J. Photochem. Photobiol., A* **2018**, *359*, 87−92.
(61) Planells, M.; Pizzotti, M.; Nichol, G. S.; Tessore, F.; Robertson, N. Effect of torsional twist on 2nd order non-linear optical activity of anthracene and pyrene tricyanofuran derivatives. *Phys. Chem. Chem. Phys.* **2014**, *16*, 23404−23411.
(62) Li, A.; Liu, Y.; Bi, C.; Xu, W.; Ma, Z.; Cui, H.; Xu, S. Pressure-dependent distinct luminescent evolutions of pyrene and TPA-Py single crystals. *Spectrochim. Acta, Part A* **2020**, *237*, 118390.
(63) Kachwal, V.; Joshi, M.; Mittal, V.; Choudhury, A. R.; Laskar, I. R. Strategic design and synthesis of AIEE (Aggregation Induced Enhanced Emission) active push-pull type pyrene derivatives for the ultrasensitive detection of explosives. *Sens. Bio-sens. Res.* **2019**, *23*, 100267.
(64) França, B. M. de.; Forero, J. S. B.; Garden, S. J.; Ribeiro, E. S.; Souza, R. D. S.; Teixeira, R. S.; Corrêa, R. J. Green fluorescence pyrene-based dye as a new π-extended system: synthesis, photophysical and theoretical studies. *Dyes Pigm.* **2018**, *148*, 444−451.
(65) Sun, N.; Su, K.; Zhou, Z.; Tian, X.; Jianhua, Z.; Chao, D.; Wang, D.; Lissel, F.; Zhao, X.; Chen, C. High-performance emission/color dual-switchable polymer-bearing pendant tetraphenylethylene (TPE) and triphenylamine (TPA) moieties. *Macromolecules* **2019**, *52*, 5131−5139.
(66) Kosco, J.; Moruzzi, F.; Willner, B.; Mcculloch, I. Photocatalysts based on organic semiconductors with tunable energy levels for solar fuel applications. *Adv. Energy Mater.* **2020**, *10*, 2001935.
(67) Babar, S. B.; Gavade, N. L.; Bhopate, D. P.; Kadam, A. N.; Kokane, S. B.; Sartale, S. D.; Gophane, A.; Garadkar, K. M.; Bhuse, V. M. An efficient fabrication of ZnO−carbon nanocomposites with enhanced photocatalytic activity and superior photostability. *J. Mater. Sci.: Mater. Electron.* **2019**, *30*, 1133−1147.

https://doi.org/10.1021/acsaem.1c02772
ACS Appl. Energy Mater. 2021, 4, 13140−13151